Nano Research

Open Access

Research Article

UV–Vis–NIR broadband self-powered Bi_2O_2Se-based semi-vertical heterojunction photodetector with high performance

Ying Li[1,2,3,4], Fan Zhang[1,2,5], Shiqiang Wang[1,2,6], Dapeng Li[1,2,6], Ying Sun[1,2,3], Zhen Gao[1,2,3], Zhonghuai Wu[1,2,6] ✉, and Dezhi Zheng[1,2,3] ✉

[1] *State Key Laboratory of Environment Characteristics and Effects for Near-space, Beijing Institute of Technology, Beijing 100081, China*
[2] *MIIT Key Laboratory of Complex-field Intelligent Exploration, Beijing Institute of Technology, Beijing 100081, China*
[3] *School of Interdisciplinary Science, Beijing Institute of Technology, Beijing 100081, China*
[4] *School of Mechatronics Engineering, Beijing Institute of Technology, Beijing 100081, China*
[5] *School of Information and Electronics, Beijing Institute of Technology, Beijing 100081, China*
[6] *School of Optics and Photonics, Beijing Institute of Technology, Beijing 100081, China*

Cite this article: *Nano Research*, **2026**, *19*, 94908400. https://doi.org/10.26599/NR.2026.94908400

ABSTRACT: Two-dimensional (2D) Bi_2O_2Se nanosheets, as an emerging ternary layered semiconductor, exhibit promising potential for photodetection owing to their moderate bandgap, high carrier mobility, and excellent environmental stability. However, their intrinsically high carrier concentration typically results in elevated dark currents and sluggish response speeds, thereby limiting further performance enhancement. To synergistically optimize both the response speed and sensitivity, we fabricated n-type Bi_2O_2Se nanosheets via chemical vapor deposition (CVD) and integrated them into a Bi_2O_2Se/InSe semi-vertical heterojunction photodetector featuring a single-sided depletion region. Benefitting from the type-II band alignment and the graphene bottom electrode, photogenerated carriers are efficiently separated and rapidly extracted. This design simultaneously shortens the carrier transit time and suppresses recombination, enabling the device to achieve high sensitivity (responsivity R of 0.47 A/W, detectivity D^* of 3.21 × 10^{12} Jones, external quantum efficiency (EQE) of 166.09%) while maintaining ultrafast response characteristics (rise/fall times of 48.5/41.7 μs). The photodetector exhibits broadband self-powered operation across ultraviolet (UV) to near-infrared wavelengths (300–1050 nm). These results highlight the significant potential of Bi_2O_2Se/InSe semi-vertical heterojunctions for high-performance, low-power, self-powered broadband photodetectors spanning the UV–visible–near infrared ray (UV–Vis–NIR) spectrum.

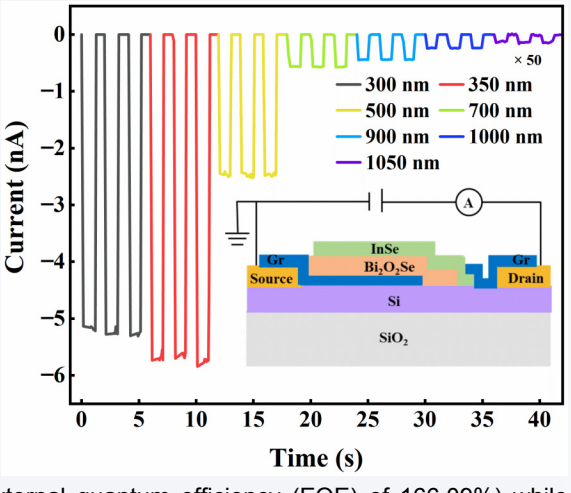

KEYWORDS: Bi_2O_2Se, two-dimensional materials, van der Waals heterostructure, self-powered, broadband, photodetector

1 Introduction

In recent years, n-type two-dimensional (2D) Bi_2O_2Se nanosheets have emerged as a promising ternary layered material due to their significant potential in photodetection application. Their crystal structure comprises alternately stacked $[Bi_2O_2]^{2+}$ layers and Se^- layers with an interlayer spacing of 0.61 nm. This unique layered arrangement helps suppress the recombination probability between electrons and holes while promoting the rapid separation and transport of photogenerated carriers, endowing the material with a series of outstanding physicochemical properties [1–4]. Bi_2O_2Se exhibits a moderate bandgap (~ 0.8 eV), an extremely low effective electron mass (approximately 0.14 m_0), and an exceptionally high intrinsic electron mobility. These properties enhance the response speed and quantum efficiency of photodetectors, endowing Bi_2O_2Se with outstanding photodetection performance [5–7]. Moreover, Bi_2O_2Se exhibits superior environmental stability compared to many other two-dimensional materials, laying the groundwork for practical applications. Based on these advantages, Bi_2O_2Se shows

Received: November 27, 2025; **Revised:** December 27, 2025
Accepted: January 1, 2026

✉Address correspondence to Zhonghuai Wu, wuzhonghuai@bit.edu.cn; Dezhi Zheng, zhengdezhi@bit.edu.cn

great prospects in optoelectronic fields such as high-speed optical communications, imaging, and contactless sensing [8–10].

However, the inherently high carrier concentration in Bi_2O_2Se readily induces elevated dark currents in devices, which not only increases power consumption but also constrains the signal-to-noise ratio (SNR) and detectivity (D^*). To address these challenges, constructing van der Waals heterojunctions (vdWHs) based on Bi_2O_2Se has emerged as an effective strategy [11–14]. The built-in electric field formed at the heterojunction interface provides a key driving force for efficient photogenerated carrier separation and self-powered operation. Although Bi_2O_2Se's high charge carrier mobility and tunable optical absorption properties offer advantages for constructing high-performance self-powered photodetectors, devices reported to date typically suffer from issues such as gain deficiency, low quantum efficiency, and slow response speed primarily due to strong carrier recombination induced by defect states [5, 15]. Furthermore, most of the existing research has focused on the visible (Vis) to near-infrared (NIR) bands [16, 17], failing to fully exploit the broad spectral response potential of Bi_2O_2Se nanosheets across the ultraviolet–visible–near-infrared (UV–Vis–NIR) spectrum. This limitation restricts their practical applications in scenarios such as multispectral detection and environmental monitoring [18].

Consequently, a Bi_2O_2Se/InSe semi-vertical heterojunction photodetector was designed in this study. The heterojunction is formed by integrating 2D InSe, which is renowned for its strong light-matter interaction and high optical absorption coefficient, with Bi_2O_2Se, which exhibits exceptionally high carrier mobility. This configuration enables self-powered broadband photodetection across the full UV–Vis–NIR spectrum [18–20]. Within the device structure, n-type Bi_2O_2Se is stacked directly atop a graphene bottom electrode, and n-type InSe is subsequently layered above the n-Bi_2O_2Se. This vertical stacking induces a single-sided depletion region within Bi_2O_2Se and a corresponding carrier accumulation region in the InSe. Such a unilateral depletion profile effectively suppresses the recombination of photogenerated carriers, thereby enhancing both responsivity and external quantum efficiency (EQE) [21, 22]. Simultaneously, the graphene electrode promotes the formation of an extended lateral depletion region within the heterostructure. Under the influence of the built-in electric field, photogenerated carriers are rapidly separated along the vertical transport channel, thereby significantly reducing both migration distance and transit time. This accelerated carrier extraction decouples optical gain from response speed—a longstanding challenge in photodetector design—and thus simultaneously enables high gain without compromising speed. Moreover, graphene exhibits high carrier mobility, which reduces contact resistance and forms an excellent ohmic contact with the materials. This minimizes series resistance and shortens carrier transit time. When employed as an electrode, graphene further suppresses recombination of photogenerated carriers while enabling rapid device response [15, 23].

Therefore, under zero bias conditions, the device exhibits outstanding performance: a high optical switching ratio of 10^4, a responsivity (R) of 0.47 A/W, a D^* of 3.21 × 10^{12} Jones, an EQE as high as 166.09%, and rise/fall times of 48.5/41.7 μs. It exhibits broadband optical response spanning ultraviolet to near-infrared (300–1050 nm), achieving high sensitivity while maintaining excellent fast response capability. Our findings provide a suitable approach for developing high-performance, self-powered photodetectors based on 2D vdWHs.

2 Results and discussion

Figure 1(a) illustrates a schematic process for growing Bi_2O_2Se using chemical vapor deposition (CVD). Bi_2O_3 and Bi_2Se_3 powders were selected as reaction precursors, with fluor mica (f-mica) serving as the growth substrate. The detailed procedure is described in the experimental section [24–26]. Optical microscope (OM) images in Fig. 1(b) present Bi_2O_2Se nanosheets grown on f-mica exhibiting square morphology with dimensions ranging from 10 to 50 μm. To confirm the material's chemical composition, X-ray

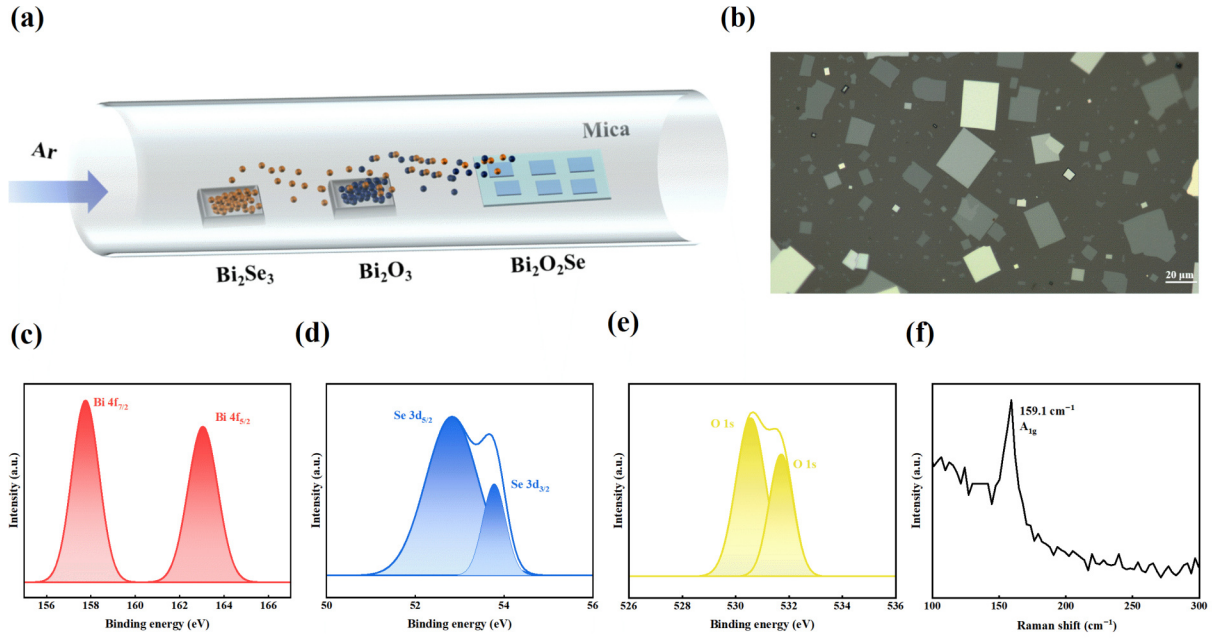

Figure 1 Synthesis and characterization of two-dimensional Bi_2O_2Se nanosheets. (a) Schematic of CVD growth of Bi_2O_2Se. (b) Optical microscope image of Bi_2O_2Se nanosheets deposited on a mica substrate. XPS spectra of Bi_2O_2Se: (c) Bi 4f, (d) Se 3d, and (e) O 1s. (f) Raman spectrum of Bi_2O_2Se nanosheets.

photoelectron spectroscopy (XPS) was employed. As shown in Figs. 1(c)–1(e), characteristic peaks appear at Bi 4f energies of 158.7 and 163.0 eV, representing Bi $4f_{7/2}$ and Bi $4f_{5/2}$, respectively. The Se $3d_{3/2}$ and Se $3d_{5/2}$ peaks in the Se spectrum are observed at 53.8 and 52.9 eV respectively, while the two characteristic peaks in the O 1s spectrum are located at 531.7 and 530.6 eV. All binding energies are in agreement with the Bi_2O_2Se composition [8, 18], confirming the chemical purity of the synthesized material. Furthermore, the Raman spectrum of two-dimensional Bi_2O_2Se (as shown in Fig. 1(f)) exhibits a single characteristic peak for the A_{1g} mode at ~ 159.1 cm^{-1}. This mode originates from the symmetric vibration of Bi–O bonds within the two back-to-back Bi_2O_2Se layers. The singlet nature and uniformity of the Raman peak further indicate that the prepared Bi_2O_2Se nanosheets exhibit excellent crystalline quality and structural homogeneity [12, 27].

The schematic diagram and the optical microscope image of the Bi_2O_2Se/InSe van der Waals heterojunction device are shown in Figs. 2(a) and 2(b). During the fabrication of the van der Waals Bi_2O_2Se/InSe heterojunction device, few-layer graphene was firstly mechanically exfoliated and transferred as the bottom electrode onto a pre-fabricated Au electrode on a SiO_2/Si substrate. Graphene, with its remarkably high mobility and excellent flexibility, effectively minimizes series resistance and reduces carrier transit time, thereby suppressing photogenerated carrier recombination and enhancing device response speed. This makes it an ideal electrode material for constructing high-quality electrode-semiconductor interfaces [28–30]. Subsequently, Bi_2O_2Se flakes were precisely transferred from a f-mica substrate onto the graphene layer using polydimethylsiloxane (PDMS) [31]. An InSe flake was then placed atop the Bi_2O_2Se flake. Finally, another graphene sheet was subsequently transferred and connected to a pre-fabricated Au electrode on the SiO_2/Si substrate, forming a semi-vertical heterojunction device with a graphene/Bi_2O_2Se/InSe/graphene structure. This fully transfer process avoided contamination potentially induced by conventional metal electrode depositions, ensuring a clean device surface and high-quality heterojunction interfaces [20]. The bottom electrode, in conjunction with the n-n semiconductor heterojunction, establishes an extended lateral single-sided depletion region. This configuration shortens both the migration distance and transit time of photogenerated carriers, suppresses recombination loss, and enables synergistic optimization of optical gain and response time.

Surface topography characterized by atomic force microscopy (AFM) scanning (Fig. 2(c)), revealed thicknesses of 19.62, 138.62, and 63.65 nm for graphene, Bi_2O_2Se, and InSe, respectively (Fig. 2(d)). To validate the formation and quality of the Bi_2O_2Se/InSe heterostructure, Raman spectroscopy characterization was performed (Fig. 2(e)). The characteristic Raman peak of Bi_2O_2Se is observed at 159.1 cm^{-1}, corresponding to the A_{1g} vibrational mode. The Raman spectrum of the InSe flake exhibits three intense peaks at 115.6, 179.4, and 228.4 cm^{-1}, corresponding to the A^1_{1g}、E^1_{2g} and A^2_{1g} modes, respectively [32, 33]. Furthermore, in graphene/Bi_2O_2Se/InSe/graphene heterojunction device, the presence of overlying Bi_2O_2Se and InSe layers significantly attenuates the Raman signal from the underlying graphene electrode. The resulting characteristic peak intensities fall below the detection limit, preventing effective extraction. Consequently, the graphene electrode was characterized by separately measuring the Raman spectrum. The inset in Fig. 2(e) displays the Raman spectrum of graphene, featuring two characteristic peaks at 1582.8 and 2718.6 cm^{-1}, corresponding to the G and 2D phonon modes of graphene, respectively [34]. The Raman peaks in the Bi_2O_2Se/InSe heterojunction region exhibit no shift compared to those of isolated Bi_2O_2Se and InSe. This observation indicates the successful

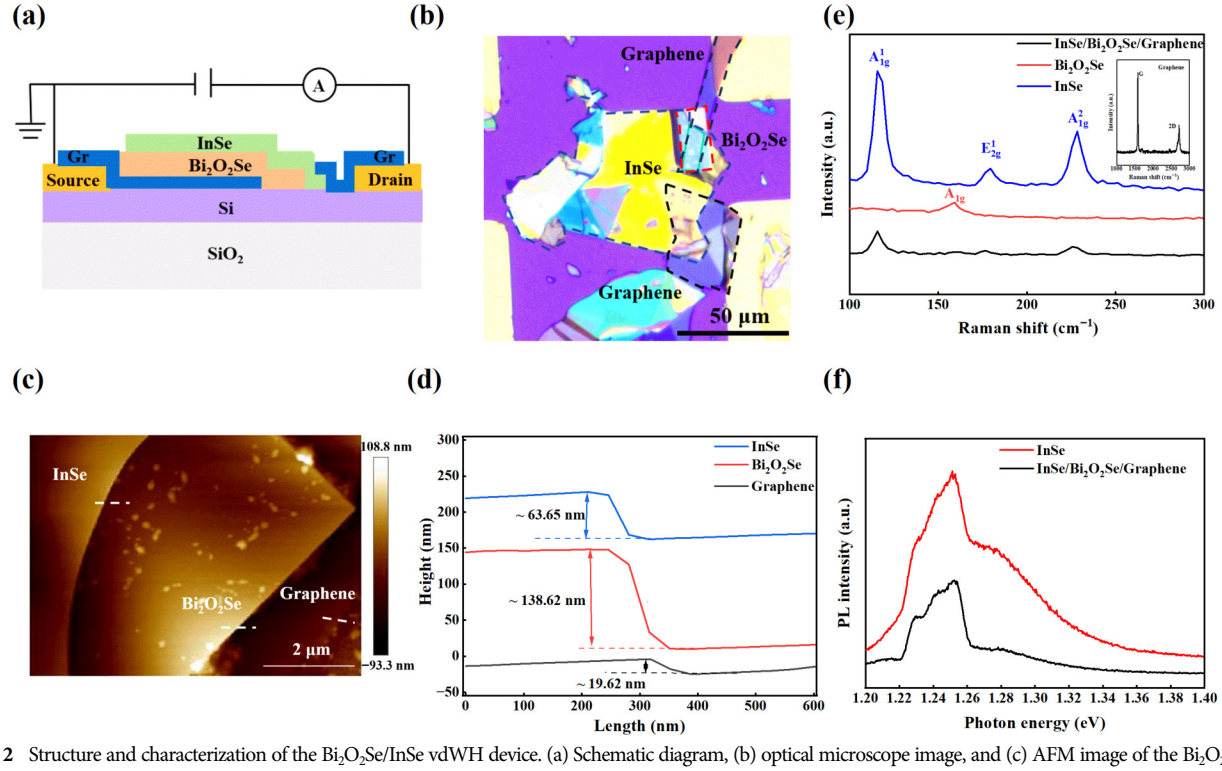

Figure 2 Structure and characterization of the Bi_2O_2Se/InSe vdWH device. (a) Schematic diagram, (b) optical microscope image, and (c) AFM image of the Bi_2O_2Se/InSe device. (d) AFM profile of the Bi_2O_2Se and InSe layers. (e) Raman spectra of the Bi_2O_2Se, InSe, and Bi_2O_2Se/InSe heterojunction regions. The inset shows the Raman spectrum of the graphene region. (f) Comparison of PL spectra between InSe nanosheet and the Bi_2O_2Se/InSe heterojunction region.

formation of a high-quality heterojunction formation. Furthermore, the photoluminescence (PL) spectrum (Fig. 2(f)) reveals an emission peak for InSe at approximately 1.25 eV. The PL intensity is significantly quenched compared to the standalone InSe region, indicating efficient exciton dissociation and interlayer charge transfer within the heterojunction. This further confirms the high quality of the constructed heterojunction [5, 20].

The transfer characteristic curves of field-effect transistors fabricated from Bi_2O_2Se and InSe single materials are shown in Fig. S1 in the Electronic Supplementary Material (ESM). All transfer curves exhibit typical n-type electron transport behavior consistent with the n-type semiconductor properties of both materials, indicating that the Bi_2O_2Se/InSe van der Waals heterojunction forms an n-n heterojunction [20]. To determine the band alignment of the Bi_2O_2Se/InSe van der Waals heterojunction device, the work functions of Bi_2O_2Se and InSe flakes were measured using Kelvin probe force microscopy (KPFM). The surface potential distribution of the heterojunction region (Fig. 3(a)) illustrates the contact potential difference (CPD) distribution between the KPFM tip and the sample, revealing a distinct surface potential difference exists between the Bi_2O_2Se and InSe regions [35, 36]. The Fermi level of InSe is approximately 67.3 meV lower than that of Bi_2O_2Se (Fig. 3(b)). Based on these results, combined with the electron affinity and bandgap of Bi_2O_2Se and InSe, the band alignment prior to heterojunction formation is established as shown in Fig. 3(c) [11, 37]. Following the formation of the Bi_2O_2Se/InSe vdWH, electrons diffuse from Bi_2O_2Se into InSe, creating an electron-rich region on the InSe side and an electron-depleted region on the Bi_2O_2Se side. Concurrently, the band structure at the interface undergoes bending. This results in the formation of a built-in electric field, as illustrated in Fig. 3(d), directed from Bi_2O_2Se towards InSe, thereby causing carrier drift. In the dark state, carrier diffusion and drift in the heterojunction region reach equilibrium, exhibiting characteristics of an n-n heterojunction and forming a unilateral depletion region. Under illumination, the photo-excited electron-hole pairs within the junction region are separated by the built-in electric field, generating a "self-driven" photocurrent without applied drain voltage (V_{ds}) or gate voltage (V_g) [38]. Figure 3(e) displays the output curves (I_{ds}–V_{ds}) of the heterojunction in dark conditions, with the drain voltage (on the InSe side) ranging from −1 to 1 V. Under reverse or zero bias, the built-in potential barrier prevents most electron transfer from InSe to Bi_2O_2Se, yielding currents below 0.68 pA. When the V_{ds} is positive, the applied electric field is opposite to the built-in electric field, weakening the latter and reducing the barrier height, thereby facilitating electron injection from the Bi_2O_2Se region into the InSe region. A dark current of 9 pA was observed under forward bias [39]. Upon illumination, photogenerated electrons and holes rapidly separated under the built-in electric field, migrating into Bi_2O_2Se and InSe respectively, generating a substantial photocurrent (Fig. 3(f)) [40].

Using a 350 nm xenon lamp as the test light source, the photoelectric performance of Bi_2O_2Se/InSe heterojunction photodetectors was systematically investigated under zero bias conditions. The I_{ds}–V_{ds} under different incident light power density (P_{inc}) are presented in Fig. 4(a). As P_{inc} increases, the I_{ds}–V_{ds} curve shifts overall to the upper right, exhibiting a significant photoresponse at zero bias and demonstrating excellent

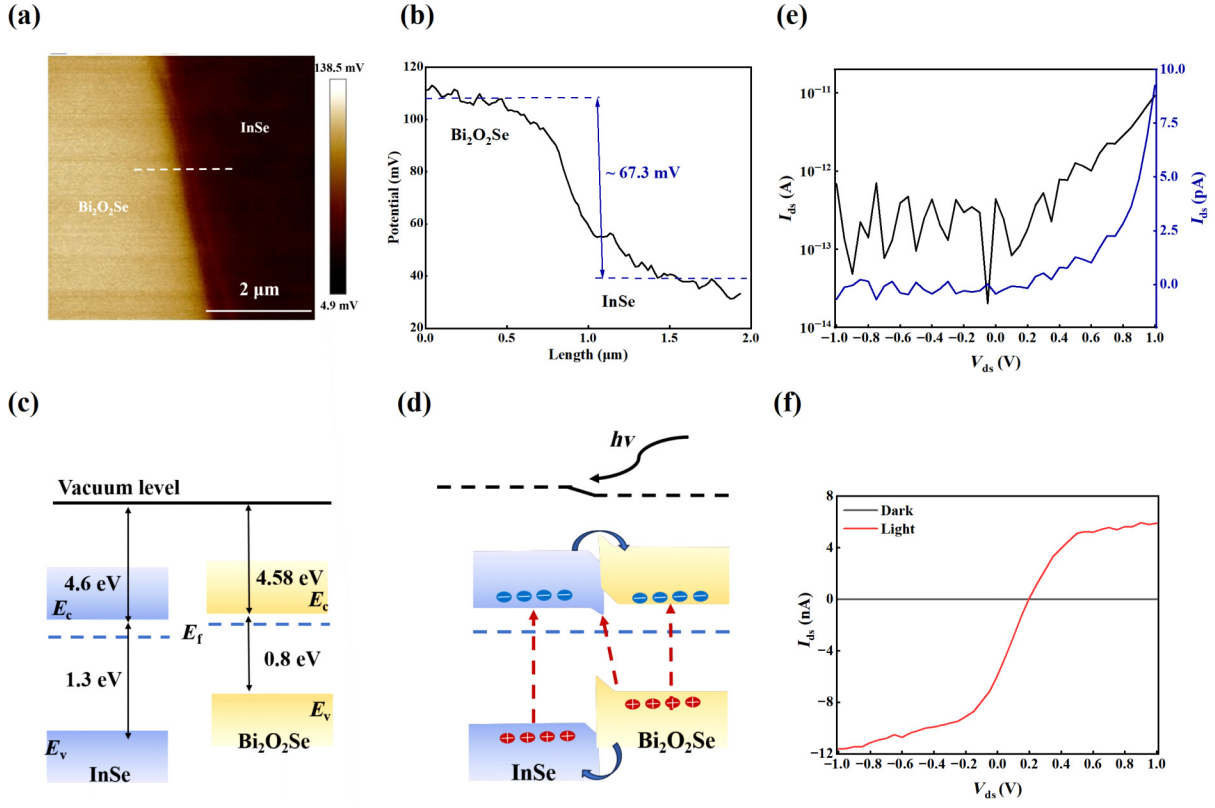

Figure 3 Band structure of the Bi_2O_2Se/InSe heterojunction. (a) Surface potential distribution map of the heterojunction region. (b) CPD between Bi_2O_2Se and InSe. (c) Schematic band diagrams of Bi_2O_2Se and InSe before contact. (d) Schematic band structure after contact under illumination. (e) I_{ds}–V_{ds} curves of the device under dark condition, with I_{ds} plotted in both linear and logarithmic formats. (f) I_{ds}–V_{ds} curves of the device under dark and illuminated conditions.

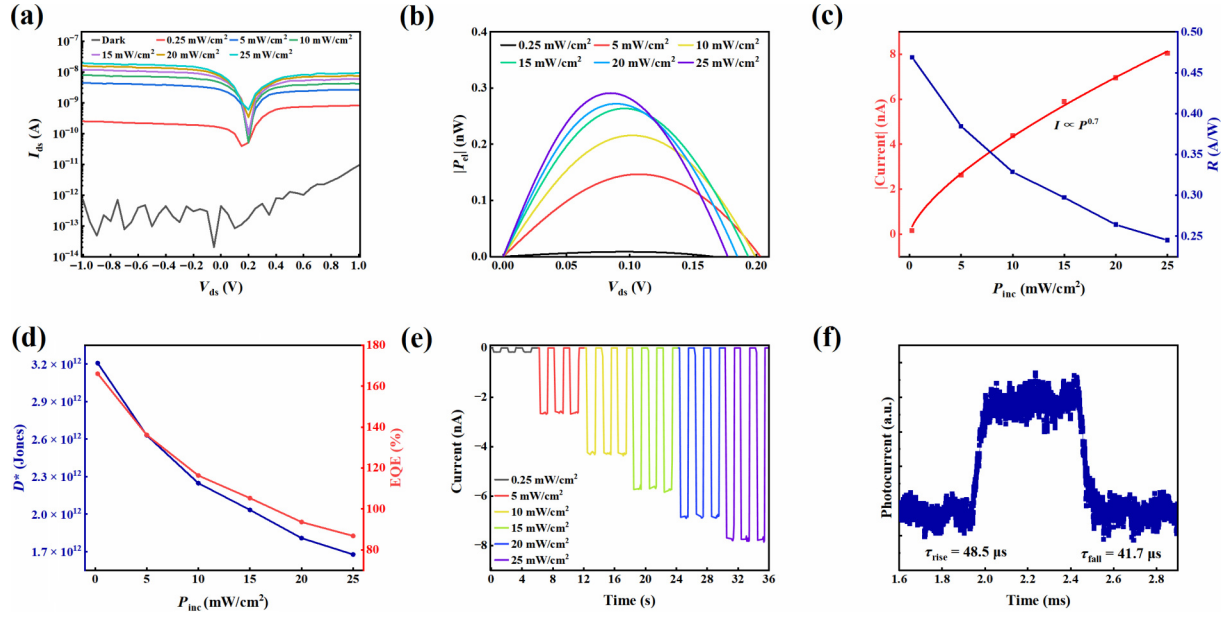

Figure 4 Photodetection performance of Bi_2O_2Se/InSe van der Waals heterostructure photodetectors under 350 nm illumination. (a) Logarithmic plots of I_{ds}–V_{ds} for the device at different P_{inc}. (b) P_{el} as a function of V_{ds} under various P_{inc}. (c) When V_{ds} = 0, the current and R at different P_{inc}. (d) When V_{ds} = 0, the D^* and EQE at different P_{inc}. (e) I–T curves at varying P_{inc} when V_{ds} = 0. (f) Transient time-resolved photoresponse curve of the Bi_2O_2Se/InSe heterojunction at V_{ds} = 0 V.

photovoltaic effect [5, 41]. As shown in Fig. 4(b), the device's output power (P_{el}), extracted using the formula as follows

$$P_{el} = I_{ds} \times V_{ds} \quad (1)$$

increases with the P_{inc}, reaching a maximum value of 0.31 nW at P_{inc} = 25 mW/cm². Furthermore, the fill factor (FF) and power conversion efficiency (PCE) are key parameters for evaluating photovoltaic performance, defined as

$$FF = \frac{P_{el,max}}{I_{sc} \times V_{oc}} \quad (2)$$

$$PCE = \frac{P_{el}}{P_{in}} \quad (3)$$

where P_{in} represents the effective incident light power [42, 43]. At P_{inc} = 0.25 mW/cm², the open-circuit voltage (V_{OC}) and short-circuit current (I_{SC}) were measured to be 0.17 V and 0.15 nA, respectively. The maximum FF and PCE were calculated to be 0.4 and 3.0%, surpassing previously reported photodetectors based on Bi_2O_2Se heterostructures [5, 16].

Subsequently, the self-powered photodetection performance of Bi_2O_2Se/InSe devices was evaluated under V_{ds} = 0 V. As shown in Fig. 4(c), the photocurrent increases with increasing incident light power density, exhibiting a power-law relationship as expressed by the following formula

$$I \propto P^{\alpha} \quad (4)$$

with a fitted exponent α of 0.7. This sublinear response may stem from partial photon non-conversion due to defects or impurities within the material and adsorbed molecules at the heterojunction interface [5, 44]. At zero bias, the dark current is as low as 0.44 pA. Under a P_{inc} of 25 mW/cm², the photocurrent reaches approximately 8.05 nA, yielding an on/off ratio (I_{light}/I_{dark}) of 1.82 × 10⁴. Key photodetection parameters such as R, D^*, and EQE are calculated using the following equations

$$R = \frac{I_{illumination} - I_{dark}}{A \times P_{inc}} \quad (5)$$

$$D^* = \frac{R \times \sqrt{A}}{\sqrt{2e \times I_{dark}}} \quad (6)$$

$$EQE = \frac{h \times C \times R}{e \times \lambda} \quad (7)$$

where A denotes the effective illumination area, while h, e, and c represent Planck's constant, the elementary charge, and the speed of light, respectively [16, 45, 46]. As illustrated in Figs. 4(c) and 4(d), at a P_{inc} of 0.25 mW/cm², R, D^*, and EQE achieve values of 0.47 A/W, 3.21 × 10¹² Jones, and 166.09%, respectively. These parameters gradually decrease with increasing P_{inc}, primarily attributed to enhanced nonradiative recombination due to defect state filling under high injection conditions, which shortens carrier lifetime [47, 48]. Nevertheless, at P_{inc} = 25 mW/cm², the device maintains excellent performance with R = 0.25 A/W, D^* = 1.68 × 10¹² Jones, EQE = 86.80%, indicating that its built-in electric field, supported by the Type-II band structure, still effectively separates photogenerated carriers. The large-area lateral single-sided depletion region formed in the heterojunction enables rapid separation of photogenerated carriers along the perpendicular depletion channel, thereby minimizing interfacial and migrational recombination loss. Concurrently, the graphene bottom electrode provides a high-mobility transport pathway that facilitates efficient extraction of photogenerated carriers, further suppressing recombination. Together, these mechanisms synergistically shorten carrier transit time, enabling both high optical gain and ultrafast photoresponse. As a result, the device exhibits exceptional optoelectronic performance. For a more accurate evaluation of the device's D^*, the detectivity D^* based on noise power spectral density is provided in the ESM (calculation of the D^*). Although this more conservative value is slightly lower than the shot-noise-limited estimate, both methodologies consistently demonstrate that the

device possesses high detection performance exceeding 10^{11} Jones (Fig. S6 in the ESM) [49, 50].

Response speed is a critical performance metric for photodetectors. At V_{ds} = 0 V, the multi-cycle time-resolved optical response curves of the device under different P_{inc} at 350 nm demonstrate excellent reproducibility and reliability (Fig. 4(e)). The response speed of the photodetector is characterized by the rise time τ_{rise} (the time taken for I_{ds} to rise from 10% to 90% of its maximum I_{ds}) and the fall time τ_{fall} (the time taken for I_{ds} to decay from 90% to 10% its maximum I_{ds}) [5]. As depicted in Fig. 4(f), the transient response curve of the self-powered Bi_2O_2Se/InSe photodetector was measured to be 48.5 and 41.7 μs respectively at a P_{inc} of 15 mW/cm^2, indicating the device possesses microsecond-level fast optical response capability. Furthermore, the device's photoelectric performance was further enhanced under applied bias, while its time-resolved response still maintained excellent reproducibility (Fig. S2 in the ESM).

Using a xenon lamp as the light source, the self-powered broadband photodetection performance of Bi_2O_2Se/InSe photodetectors across the UV–Vis–NIR spectrum ranging from 300 to 1050 nm was further investigated. As shown in Fig. 5(a), under a constant P_{inc} of 15 mW/cm^2, the device exhibits distinct I_{ds}–V_{ds} photovoltaic responses across representative wavelengths from 300 to 1050 nm, demonstrating robust broadband detection capability. The multi-cycle time-resolved optical response curves of the device across the 300–1050 nm wavelength range under a constant light intensity, are shown in Fig. 5(b), demonstrating excellent repeatability and stability. Furthermore, the spectral response performance of the device was quantitatively evaluated through parameters such as R, D^*, and EQE, as shown in Figs. 5(c) and 5(d). Due to the synergistic and competitive interactions between the intrinsic bandgap absorption of Bi_2O_2Se and InSe materials and the interlayer transition mechanism characteristic of the type-II heterojunction, the photoresponse performance initially increases before diminishing. This occurs because the strong intrinsic absorption of high-energy photons by the InSe layer reaches its maximum at 350 nm. As the incident light wavelength increases, the photon energy decreases, leading to a reduction in the optical absorption coefficient and a consequent drop in photoresponse. The slight enhancement observed near 950–975 nm is a hallmark of the type-II band alignment, signifying interlayer transitions. Specifically, photons with energies near the interlayer transition effectively drive electrons from the valence band of Bi_2O_2Se across the heterointerface into the conduction band of InSe. This spatially indirect transition yields a localized increase in photocurrent due to its high intrinsic carrier collection efficiency. Beyond 975 nm, the photoresponse is predominantly governed by the intrinsic absorption of the narrow-bandgap Bi_2O_2Se, resulting in a gradual attenuation with increasing wavelengths [5, 51].

To further validate the device's detection performance across the ultraviolet to near-infrared bands, representative wavelengths of 350, 500, and 975 nm were selected for detailed characterization. It was found that the device exhibited excellent photovoltaic characteristics across all bands (corresponding to 350 nm in Fig. 4, as well as 500 and 975 nm in Figs. S3 and S4 in the ESM, respectively). These results collectively demonstrate that the Bi_2O_2Se/InSe heterojunction photodetector possesses stable and highly efficient self-powered photodetection capabilities across a

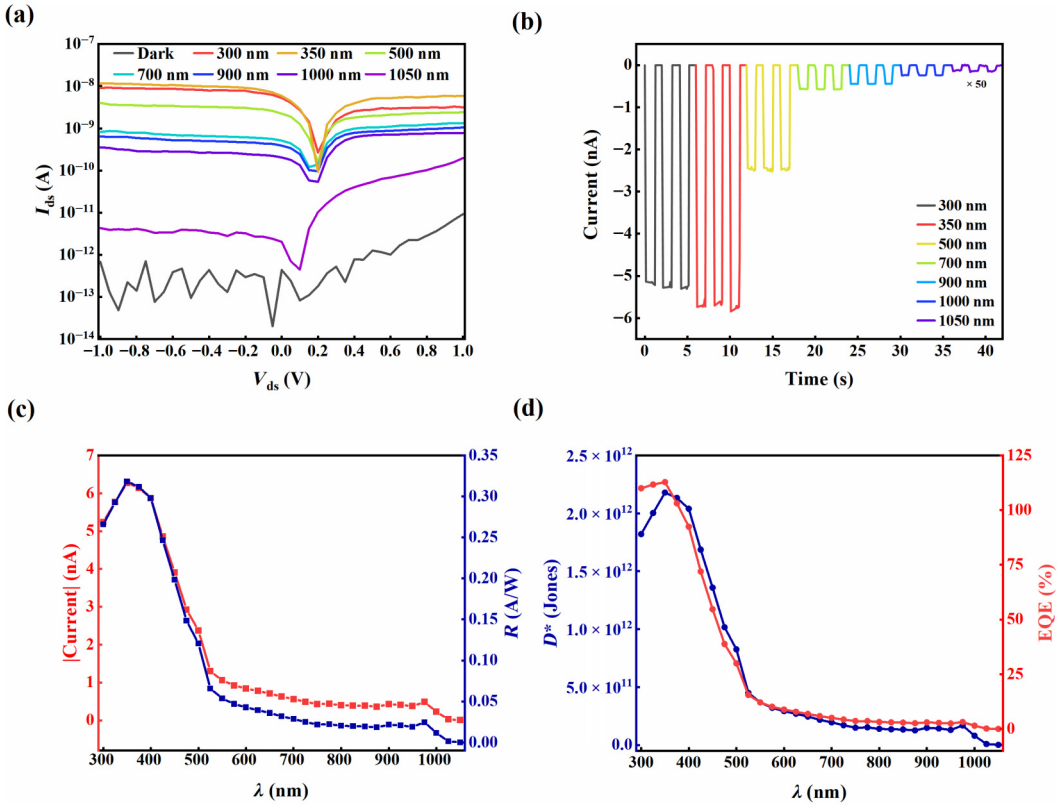

Figure 5 Broadband self-powered photodetection characteristics of Bi_2O_2Se/InSe vdWH photodetectors. (a) I_{ds}–V_{ds} curves of the device under different wavelengths at a P_{inc} of 15 mW/cm^2. (b) I–T curves at V_{ds} = 0 for different wavelengths under a P_{inc} of 15 mW/cm^2. (c) Relationship between photocurrent and R with wavelength at zero bias. (d) Relationship between D^* and EQE with wavelength at zero bias.

broad spectral range of 300–1050 nm, exhibiting outstanding full-band photoresponse performance.

Bi_2O_2Se/InSe photodetector, with its fast optical response and self-powered characteristics, has demonstrated significant application potential in the field of optical communications. To evaluate the performance of the designed semi-vertical heterojunction photodetector, we constructed a UV–Vis–NIR optical communication system, as shown in Fig. 6(a). A xenon lamp serves as the broadband source, whose output is modulated by a programmable shutter to encode the optical signal. The ASCII-encoded digital information is converted into corresponding control signals that drive the shutter, generating optical pulses corresponding to a binary sequence across the UV–Vis–NIR spectrum. At the receiving end, the Bi_2O_2Se/InSe photodetector converts the incident light pulses into photocurrent signals, which are recorded and decoded in real-time by a computer to reconstruct the transmitted information [39, 40].

As shown in Fig. 6(b), representative wavelengths—350, 500, and 850 nm—were selected to demonstrate the detector's broadband operation. Under illumination at these wavelengths, the detector successfully produced clear and stable photocurrent response signals corresponding to the shutter-encoded letter "BIT". The output signal faithfully reproduced the original input, confirming high-quality optical communication [52]. These results underscore the practical applicability of the self-powered Bi_2O_2Se/InSe photodetector in UV–Vis–NIR optical communication systems.

Key parameters of the Bi_2O_2Se/InSe semi-vertical photodetector are summarized in Table 1 and compared with several Bi_2O_2Se-based and other heterojunction self-driven photodetectors reported in the literature. The Bi_2O_2Se/InSe semi-vertical photodetector exhibits outstanding R and D^*, EQE values, and response speed under zero bias, demonstrating exceptional broadband self-powered optical response performance spanning the ultraviolet to near-infrared spectrum (300–1050 nm).

3 Conclusions

In summary, we have successfully designed and fabricated a Bi_2O_2Se/InSe semi-vertical heterojunction photodetector based on CVD-grown n-type Bi_2O_2Se nanosheets. The device exhibits exceptional self-powered broadband photoresponse across 300–1050 nm, enabled by the synergistic integration of a single-sided depletion region and a graphene electrode. This architecture simultaneously achieves high sensitivity (R = 0.47 A/W, D^* = 3.21 × 10^{12} Jones, EQE = 166.09%) and microsecond-scale response speeds (rise/fall times of 48.5/41.7 μs). These results underscore the compelling potential of semi-vertical van der Waals heterojunctions as a versatile platform for next-generation, high-performance, self-powered optoelectronic devices.

4 Experimental section

4.1 Preparation of two-dimensional Bi_2O_2Se films

Two-dimensional Bi_2O_2Se nanosheets were synthesised via CVD in a quartz tube. Bi_2O_3 powder (Alfa Aesar, 99.999%) and Bi_2Se_3 powder (Alfa Aesar, 99.999%) were placed at the thermal centre of the tube and 8 cm above it, respectively. Newly exfoliated f-mica substrates were positioned 10–14 cm downstream from the thermal center. Prior to growth, the vacuum-drawn quartz tube was repeatedly purged with high-purity argon gas (99.99%) to prevent environmental contamination. Then it was heated at a rate of 15 °C/min to 750–780 °C, held for 20 min, and allowed to cool to room temperature. In the growth process, argon gas at 150 sccm was introduced as a carrier gas to transport the precursor vapors for deposition onto the surface of the low-temperature f-mica substrates [24, 26].

4.2 Device fabrication

Bi_2O_2Se/InSe van der Waals heterojunction devices were fabricated

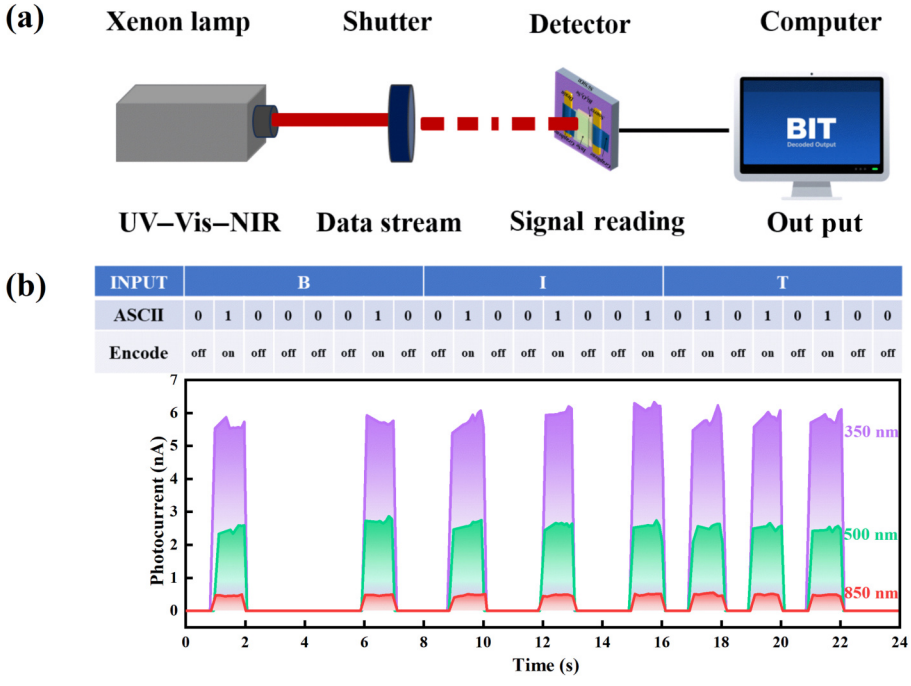

Figure 6 An optical communication system using a Bi_2O_2Se/InSe photodetector. (a) Schematic diagram of the system. (b) Input and output signals showing the transmission of the ASCII code "BIT" in the Bi_2O_2Se/InSe optical communication system.

Table 1 Comparison of performance with previously published self-powered photodetectors based on Bi_2O_2Se and other heterojunctions

Materials	Wavelength (nm)	R (A/W)	D^* (Jones)	EQE (%)	T (μs)	Reference
Bi_2O_2Se/InSe	300–1050	0.47	3.21×10^{12}	166.09	48.5/41.7	This Work
Bi_2O_2Se/InSe	400–1064	0.075	1.08×10^{12}	23.05	$5.8/15 \times 10^3$	[5]
Bi_2O_2Se/WSe_2	532	0.28	—	66.27	20/20	[53]
Bi_2O_2Se/$MoTe_2$	532	0.33	—	78.10	—	[16]
Bi_2O_2Se/MoO_3	405–1550	0.51	6.42×10^{10}	—	80/90	[54]
Bi_2O_2Se/1D-$MoSe_2$	405–808	0.66	1.68×10^{10}	126	350/380	[17]
Bi_2O_2Se/Bi_2Se_3	532–1450	6.43×10^{-5}	10^7	—	$274/318 \times 10^3$	[55]
WS_2/InSe	325–980	0.061	2.50×10^{11}	14.5	63/76	[20]
InSe/$MoTe_2$	405	0.0879	2.9×10^{11}	27	19/14	[32]
MoS_2/WS_2	405–800	0.283	6.44×10^{12}	60.59	$375/6 \times 10^3$	[56]
WSe_2/WS_2	400–1550	0.32	6.15×10^{13}	76	$2.3/2.5 \times 10^3$	[35]
$PdSe_2$/2H-$MoTe_2$	375–1550	0.243	6.46×10^{10}	56.73	$3.5/3.7 \times 10^3$	[45]

via mechanical exfoliation and a fully dry transfer technique. First, patterned Cr/Au (10/50 nm) electrodes were fabricated on a silicon substrate covered with 300 nm SiO_2 using UV lithography and thermal evaporation processes. Subsequently, Bi_2O_2Se films were directly exfoliated from f-mica using PDMS films, avoiding contamination and structural damage potentially introduced by wet transfer methods. Graphene and InSe multilayer flakes were also mechanically exfoliated using PDMS. Subsequently, a transfer platform was employed to precisely sequentially transfer graphene, Bi_2O_2Se, InSe, and graphene back onto the SiO_2/Si substrate, constructing a vdWH Bi_2O_2Se/InSe semi-vertical photodetector with graphene as the bottom electrode. Finally, annealing for 30 min at 200 °C under vacuum was performed to relieve stresses introduced during transfer and enhance electrode contact performance.

4.3 Device characterization

XPS spectra of Bi_2O_2Se were measured using a PHI Quantera II X-ray photoelectron spectrometer. Raman spectra were acquired at room temperature using an Alpha300R system with an excitation wavelength of 532 nm. Sample thickness and CPD were measured using a multifunctional atomic force microscope (Bruker Dimension Icon) equipped with AFM and KPFM functional modules. Photovoltaic performance testing was conducted using a Metatest E2-Vac vacuum micro-photovoltaic testing system. This system, equipped with a xenon lamp light source and a semiconductor parameter analyzer (Keithley 4200-SCS), enabled precise measurement of photovoltaic signals. All measurements were performed at room temperature.

Electronic Supplementary Material: Supplementary material (transfer curves of individual Bi_2O_2Se and InSe flakes; photodetection performance of the Bi_2O_2Se/InSe heterojunction device under different bias voltages; photodetection characteristics of the Bi_2O_2Se/InSe vdWH photodetector under 500 and 975 nm illuminations; calculation of the D^*; comparison of D^* calculated via two methods) is available in the online version of this article at https://doi.org/10.26599/NR.2026.94908400.

Data availability

All data needed to support the conclusions in the paper are presented in the manuscript and the Electronic Supplementary Material. Additional data related to this paper may be requested from the corresponding author upon request.

Acknowledgements

This work was granted by the Beijing Outstanding Young Scientist Program (No. JWZ020240101014).

Declaration of competing interest

All the contributing authors report no conflict of interests in this work.

Author contribution statement

Y. L.: Data curation, project administration, validation, writing manuscript, experimental design, conceptualization. F. Z. and S. Q. W.: Data curation. D. P. L., Y. S., Z. G., and D. Z. Z.: Project administration, funding acquisition. Z. H. W.: Project administration, funding acquisition, writing manuscript, conceptualization, supervision. All the authors have approved the final manuscript.

Use of AI statement

None.

References

[1] Yin, J. B.; Tan, Z. J.; Hong, H.; Wu, J. X.; Yuan, H. T.; Liu, Y. J.; Chen, C.; Tan, C. W.; Yao, F. R.; Li, T. R. et al. Ultrafast and highly sensitive infrared photodetectors based on two-dimensional oxyselenide crystals. *Nat. Commun.* **2018**, *9*, 3311.

[2] Wen, K. Y.; Liu, D. L.; Zhai, H. Y.; Wang, C.; Zhang, L. B.; Gao, W. S.; Liu, X.; Tian, M. L.; Wang, S. G.; Chen, X. G. Fast photothermoelectric response in CVD-grown two-dimensional Bi_2O_2Se nanoplates. *ACS Appl. Electron. Mater.* **2025**, *7*, 2537–2545.

[3] Wan, X.; Wang, X.; Yu, Y. D.; Liu, T. A.; Zhang, M. K.; Chen, E. Z.; Chen, K.; Wang, S. T.; Shao, F.; Gu, X. F. et al. Bi_2O_2Se nanoplates for lateral memristor devices. *ACS Appl. Nano Mater.* **2025**, *8*, 2260–2268.

[4] Li, M. L.; Chen, P.; Zhao, Y.; Zhao, M.; Leng, H. Q.; Wang, Y.; Ali, S.; Raziq, F.; Wu, X. Q.; Yi, J. B. et al L. Materials properties and

device applications of semiconducting bismuth oxyselenide. *InfoMat* **2024**, *6*, e12539.

[5] Zhang, Z. Y.; Han, L. X.; Dan, Z. Y.; Li, H. Y.; Yang, M. M.; Sun, Y. M.; Zheng, Z. Q.; Huo, N. J.; Luo, D. X.; Gao, W. et al. Type II homotype Bi_2O_2Se nanosheet/InSe nanoflake heterostructures for self-driven broadband visible-near-infrared photodetectors. *ACS Appl. Nano Mater.* **2023**, *6*, 4573–4583.

[6] Gou, J.; Yang, X. T.; Yu, H.; Yu, H.; Wei, Y. C.; Fu, Z. Y.; Wei, L. J.; Wang, Z. X.; Han, J. Y.; Wu, Z. M. et al. 2D ReS_2/3D Bi_2O_2Se homo-heterojunction photodetector toward near-infrared polarization sensitive detection and high sensitivity communication. *Laser Photon. Rev.* **2025**, *19*, 2500577.

[7] Zhao, Y. J.; Lou, Z. F.; Hu, J. M.; Li, Z. S.; Xu, L. X.; Chen, Z.; Xu, Z. K.; Wang, T.; Wu, M. Q.; Ying, H. T. et al. Scalable layer-controlled oxidation of Bi_2O_2Se for self-rectifying memristor arrays with sub-pA sneak currents. *Adv. Mater.* **2024**, *36*, 2406608.

[8] Zhang, B.; Liu, W. J.; Wang, Z. X.; Xie, Y. E.; Chen, Y. P. Mixed-dimensional heterostructure photodetector based on Bi_2O_2Se nanosheets and PbS quantum dots. *Appl. Sci.* **2024**, *14*, 5914.

[9] Yip, W. H.; Fu, Q. D.; Wu, J.; Hippalgaonkar, K.; Liu, Z.; Wang, X. L.; Boutchich, M.; Tay, B. K. Few-layer Bi_2O_2Se: A promising candidate for high-performance near-room-temperature thermoelectric applications. *Nanotechnology* **2024**, *35*, 465401.

[10] Xie, H. R.; Yang, T. F.; Xie, M. Y.; Liang, X. J.; Fang, Z. L.; Ye, Y.; Chen, Y.; Wei, Y. M.; Wang, Z.; Guan, H. Y. et al. Dual-crossbar configurated Bi_2O_2Se device for multiple optoelectronic applications. *Laser Photon. Rev.* **2024**, *18*, 2301129.

[11] Wei, L. J.; Wu, Z. M.; Wei, Y. C.; Li, C. Y.; Fu, Z. Y.; Han, J. Y.; Yang, X. T.; Xie, J. L.; Tian, Z. X.; Zhou, H. X. et al. High-gain and tunable linear photodetection in 2D tunneling heterostructures through potential engineering. *Adv. Funct. Mater.* **2024**, *34*, 2411736.

[12] Wang, D.; Wu, Q.; Shan, K. H.; Han, M. W.; Jiang, W. Y.; Meng, W. T.; Zhang, Y. Q.; Xiong, W. M. Enhanced photoelectric performance of Bi_2O_2Se/$CuInP_2S_6$ heterojunction via ferroelectric polarization in two-dimensional $CuInP_2S_6$. *Phys. Chem. Chem. Phys.* **2024**, *26*, 21357–21364.

[13] Lu, F. C.; Gao, J.; Yang, H.; Zhao, Q.; Deng, J. J.; Liu, X. L.; Wang, W. J.; Fan, S. D. High performance photodetector based on WSe_2 p-n homojunction induced by the electron doping from Bi_2O_2Se. *Physica E: Low-Dimens. Syst. Nanostruct.* **2024**, *158*, 115907.

[14] Wang, G. C.; Liu, F. J.; Chen, R. C.; Wang, M. X.; Yin, Y. X.; Zhang, J.; Sa, Z. X.; Li, P. S.; Wan, J. C.; Sun, L. et al. Tunable contacts of Bi_2O_2Se nanosheets msm photodetectors by metal-assisted transfer approach for self-powered near-infrared photodetection. *Small* **2024**, *20*, 2306363.

[15] Yang, S. Q.; Wu, Z. T.; Wang, S. L.; Zheng, P.; Zhang, Y. Significantly enhanced photoresponse of self-powered 2D MoS_2/WS_2 heterojunction photodiode via F4-TCNQ doping. *ACS Appl. Electron. Mater.* **2024**, *6*, 3374–3384.

[16] Sun, L.; Xu, Y. S.; Yin, T. T.; Wan, R.; Ma, Y. A.; Su, J.; Zhang, Z.; Liu, N. S.; Li, L. Y.; Zhai, T. Y. et al. Van der Waals heterostructure of Bi_2O_2Se/$MoTe_2$ for high-performance multifunctional devices. *Nano Energy* **2024**, *119*, 109047.

[17] Chen, Z. C.; Huang, J. M.; Yang, M. M.; Liu, X.; Zheng, Z. Q.; Huo, N. J.; Han, L. X.; Luo, D. X.; Li, J. B.; Gao, W. Bi_2O_2Se nanowire/$MoSe_2$ mixed-dimensional polarization-sensitive photodiode with a nanoscale ultrafast-response channel. *ACS Appl. Mater. Interfaces* **2023**, *15*, 30504–30516.

[18] Tong, T.; Chen, Y. F.; Qin, S. C.; Li, W. S.; Zhang, J. R.; Zhu, C. H.; Zhang, C. C.; Yuan, X.; Chen, X. Q.; Nie, Z. H. et al. Sensitive and ultrabroadband phototransistor based on two-dimensional Bi_2O_2Se nanosheets. *Adv. Funct. Mater.* **2019**, *29*, 1905806.

[19] Khan, U.; Nairan, A.; Khan, K.; Li, S. A.; Liu, B. L.; Gao, J. K. Salt-assisted low-temperature growth of 2D Bi_2O_2Se with controlled thickness for electronics. *Small* **2023**, *19*, 2206648.

[20] Chen, J. P.; Zhang, Z.; Ma, Y.; Feng, J. Y.; Xie, X. Y.; Wang, X. X.; Jian, A. Q.; Li, Y. Z.; Li, Z. X.; Guo, H. et al. High-performance self-powered ultraviolet to near-infrared photodetector based on WS_2/InSe van der Waals heterostructure. *Nano Res.* **2023**, *16*, 7851–7857.

[21] Ahn, J.; Ko, K.; Kyhm, J. H.; Ra, H. S.; Bae, H.; Hong, S.; Kim, D. Y.; Jang, J. S.; Kim, T. W.; Choi, S. et al. Near-infrared self-powered linearly polarized photodetection and digital incoherent holography using WSe_2/$ReSe_2$ van der Waals heterostructure. *ACS Nano* **2021**, *15*, 17917–17925.

[22] Wang, Y. C.; Wu, Z. T.; Zheng, P.; Zhang, Y. High-performance and broadband 2D ReS_2/MoS_2 semivertical heterojunction photodiodes. *Mater. Sci. Semicond. Process.* **2023**, *165*, 107650.

[23] Chen, Z. S.; Zhang, Z. L.; Biscaras, J.; Shukla, A. A high performance self-driven photodetector based on a graphene/InSe/MoS_2 vertical heterostructure. *J. Mater. Chem. C* **2018**, *6*, 12407–12412.

[24] Luo, P.; Zhuge, F. W.; Wang, F. K.; Lian, L. Y.; Liu, K. L.; Zhang, J. B.; Zhai, T. Y. PbSe quantum dots sensitized high-mobility Bi_2O_2Se nanosheets for high-performance and broadband photodetection beyond 2 μm. *ACS Nano* **2019**, *13*, 9028–9037.

[25] Yang, T.; Li, X.; Wang, L. M.; Liu, Y. M.; Chen, K. J.; Yang, X.; Liao, L.; Dong, L.; Shan, C. X. Broadband photodetection of 2D Bi_2O_2Se–$MoSe_2$ heterostructure. *J. Mater. Sci.* **2019**, *54*, 14742–14751.

[26] Wu, J. X.; Liu, Y. J.; Tan, Z. J.; Tan, C. W.; Yin, J. B.; Li, T. R.; Tu, T.; Peng, H. L. Chemical patterning of high-mobility semiconducting 2D Bi_2O_2Se crystals for integrated optoelectronic devices. *Adv. Mater.* **2017**, *29*, 1704060.

[27] Gao, S. M.; Wu, X. Q.; Xiao, X. F.; Liu, W. L.; Huang, K. Direct growth Bi_2O_2Se nanosheets on SiO_2/Si substrate for high-performance and broadband photodetector. *Nanotechnology* **2024**, *35*, 125703.

[28] Dai, M. J.; Chen, H. Y.; Wang, F. K.; Long, M. S.; Shang, H. M.; Hu, Y. X.; Li, W.; Ge, C. Y.; Zhang, J.; Zhai, T. Y. et al. Ultrafast and sensitive self-powered photodetector featuring self-limited depletion region and fully depleted channel with van der Waals contacts. *ACS Nano* **2020**, *14*, 9098–9106.

[29] Gao, W.; Zheng, Z. Q.; Li, Y. T.; Xia, C. X.; Du, J.; Zhao, Y.; Li, J. B. Out of plane stacking of InSe-based heterostructures towards high performance electronic and optoelectronic devices using a graphene electrode. *J. Mater. Chem. C* **2018**, *6*, 12509–12517.

[30] Wu, J. F.; Zhang, J. L.; Jiang, R. Q.; Wu, H.; Chen, S. H.; Zhang, X. L.; Wang, W. H.; Yu, Y. F.; Fu, Q.; Lin, R. et al. High-sensitivity, high-speed, broadband mid-infrared photodetector enabled by a van der Waals heterostructure with a vertical transport channel. *Nat. Commun.* **2025**, *16*, 564.

[31] Wu, J. H.; Wei, M. L.; Mu, J. L.; Ma, H.; Zhong, C. Y.; Ye, Y. T.; Sun, C. L.; Tang, B.; Wang, L. C.; Li, J. Y. et al. High-performance waveguide-integrated Bi_2O_2Se photodetector for Si photonic integrated circuits. *ACS Nano* **2021**, *15*, 15982–15991.

[32] He, S. X.; Huang, Y. X.; Yin, C. D.; Ma, Y. P.; Shan, A. D.; Wei, T. R.; Li, M.; Zhao, L. C.; Gao, L. M. Self-powered and vis-infrared broadband Gr/InSe/$MoTe_2$ heterostructure photodetectors with ultra-fast response and low dark current. *Laser Photon. Rev.* **2025**, *19*, 2400480.

[33] Zhang, W. Y.; Chiao, K. H.; Huang, H. W.; Abid, M.; Ó Coileáin, C.; Hung, K. M.; Chang, C. R.; Wu, Y. R.; Wu, H. C. Broadband InSe/MoS_2 type-II heterojunction photodetector with gate-tunable polarity induced near-linear wavelength-dependent photocurrent peak. *ACS Appl. Mater. Interfaces* **2025**, *17*, 12941–12951.

[34] Li, Y. Z.; Pan, J. Y.; Yan, C. X.; Li, J. X.; Xin, W.; Zhang, Y. T.; Liu, W. Z.; Liu, X. F.; Xu, H. Y.; Liu, Y. C. Efficient carrier multiplication in self-powered near-ultraviolet γ-InSe/graphene heterostructure photodetector with external quantum efficiency exceeding 161%. *Nano Lett.* **2024**, *24*, 7252–7260.

[35] Zhou, J. G.; Chen, W. Q.; Lu, L. D.; Zhu, B. F.; Ren, G. H.; Pan, Y. T.; Ou, J. Z.; Zhu, L. Q. Interlayer transition induced infrared response in WSe_2/WS_2 van der Waals heterostructure photodetectors with polarization and self-powered effects. *Adv. Opt. Mater.* **2025**, *13*, 2403253.

[36] Chen, M. F.; Chen, X. Q.; Wu, Z. Q.; Huang, Z. H.; Gao, W.; Yang, M. M.; Xiao, Y.; Zhao, Y.; Zheng, Z. Q.; Yao, J. D. et al. An ultrasensitive Bi_2O_2Se/In_2S_3 photodetector with low detection limit and fast response toward high-precision unmanned driving. *ACS Nano* **2024**, *18*, 27579–27589.

[37] Zhao, S. W.; Wu, J. C.; Jin, K.; Ding, H. Y.; Li, T. S.; Wu, C. Z.; Pan, N.; Wang, X. P. Highly polarized and fast photoresponse of black phosphorus-InSe vertical p-n heterojunctions. *Adv. Funct. Mater.* **2018**, *28*, 1802011.

[38] Liu, W. J.; Wu, Y. F.; Bao, X. Z. D.; Sun, L.; Xie, Y. E.; Chen, Y. P. High-performance infrared self-powered photodetector based on 2D van der Waals heterostructures. *Adv. Funct. Mater.* **2025**, *35*, 2421525.

[39] He, S. X.; Yin, C. D.; Zhang, L. L.; Chen, Y. F.; Peng, H.; Shan, A. D.; Zhao, L. C.; Gao, L. M. All-2D asymmetric self-powered photodetectors with ultra-fast photoresponse based on gr/WSe_2/$NbSe_2$ van der Waals heterostructure. *J. Mater. Sci. Technol.* **2025**, *219*, 205–212.

[40] Wang, S. F.; Wang, X. X.; Wang, W. H.; Han, T.; Li, F.; Shan, L.; Long, M. S. Unipolar barrier photodetectors based on van der Waals heterostructure with ultra-high light on/off ratio and fast speed. *Adv. Sci.* **2025**, *12*, 2413844.

[41] Li, Y. X.; He, S. X.; Yin, C. D.; Du, Y. A.; Zhao, L. C.; Gao, L. M. Realizing ultrafast respond speed and high detectivity for gate-modulated self-powered photodetector with $NbSe_2/MoS_2$ van der Waals heterostructure. *ACS Appl. Mater. Interfaces* **2025**, *17*, 31096–31106.

[42] Gan, W.; Ming, L.; Zhang, C. T.; Peng, G. H.; Cao, Z. Y.; Chen, Z.; Li, Y.; Wu, C. Q.; Liu, X.; Song, L. Self-powered broadband UV-NIR polarization-sensitive photodetector based on unipolar van der Waals heterostructure. *ACS Appl. Mater. Interfaces* **2025**, *17*, 34086–34095.

[43] Xu, J. P.; Luo, X. G.; Lin, X.; Zhang, X.; Liu, F.; Yan, Y. T.; Hu, S. Q.; Zhang, M. W.; Han, N. N.; Gan, X. T. et al. Approaching the robust linearity in dual-floating van der Waals photodiode. *Adv. Funct. Mater.* **2024**, *34*, 2310811.

[44] Fang, C. C.; Han, J. F.; Yu, M.; Liu, W. L.; Gao, S. M.; Huang, K. WS_2/Bi_2O_2Se van der Waals heterostructure with straddling band configuration for high performances and broadband photodetector. *Adv. Mater. Interfaces* **2022**, *9*, 2102091.

[45] Che, M. Q.; Wang, B.; Zhao, X. Y.; Li, Y. H.; Chang, C. L.; Liu, M. X.; Du, Y.; Qi, L. J.; Zhang, N.; Zou, Y. T. et al. $PdSe_2$/2H–$MoTe_2$ heterojunction self-powered photodetector: Broadband photodetection and linear/circular polarization capability. *ACS Nano* **2024**, *18*, 30884–30895.

[46] Xue, J. J.; Wang, X.; Xu, G. Y.; Tao, X. Y.; Pan, T. D.; Chen, Z. Y.; Cai, Q.; Shao, P. F.; Yang, G. F.; Huang, Z. L. et al J. Multiple exciton generation boosting over 100% quantum efficiency photoelectrochemical photodetection. *Nat. Commun.* **2025**, *16*, 5275.

[47] Wang, D. Z.; Li, H. Y.; Liu, J. Z.; Qin, Y.; Zhao, J. Y.; Hou, P. F. Asymmetric schottky contacts enhanced two-dimensional heterojunctions for self-powered broadband and polarization-sensitive photodetection. *ACS Appl. Mater. Interfaces* **2025**, *17*, 33089–33097.

[48] Zhan, Y. X.; Wu, Z. T.; Zeng, P. Y.; Wang, W. H.; Jiang, Y.; Zheng, H.; Zheng, P.; Zheng, L.; Zhang, Y. High-performance self-powered WSe_2/ReS_2 photodetector enabled via surface charge transfer doping. *ACS Appl. Mater. Interfaces* **2023**, *15*, 55043–55054.

[49] Shi, D. F.; Chen, J. W.; Zhu, M. L.; Guo, Z. J.; He, Z. X.; Li, M.; Wu, D.; Wang, Y. J.; Li, L. Computing imaging in shortwave infrared bands enabled by $MoTe_2$/Si 2D-3D heterojunction-based photodiode. *InfoMat* **2024**, *6*, e12618.

[50] Liu, M. X.; Wei, J. X.; Qi, L. J.; An, J. R.; Liu, X. S.; Li, Y. H.; Shi, Z. M.; Li, D. B.; Novoselov, K. S.; Qiu, C. W. et al. Photogating-assisted tunneling boosts the responsivity and speed of heterogeneous WSe_2/Ta_2NiSe_5 photodetectors. *Nat. Commun.* **2024**, *15*, 141.

[51] Su, C.; Li, M. Y.; Yan, H.; Zhang, Y.; Li, H.; Fan, W. H.; Bai, W. J.; Liu, X. J.; Wang, Q. G.; Yin, S. G. $PdSe_2/NbSe_2$ heterojunction photodetector with broadband detection and polarization sensitivity. *ACS Appl. Mater. Interfaces* **2025**, *17*, 5213–5222.

[52] Ma, X. F.; Wang, Z. P.; Qin, Q. G.; Chen, J. W.; Liu, X.; Zou, F. X.; Xu, Z. Y.; Chen, W.; Li, G. H.; Li, Y. et al. Simultaneous AoLP and DoLP detection in a bias-switchable $PdSe_2/MoS_2/PdSe_2$ heterojunction for polarization discrimination. *Adv. Mater.* **2025**, *37*, 2500572.

[53] Luo, P.; Wang, F. K.; Qu, J. Y.; Liu, K. L.; Hu, X. Z.; Liu, K. W.; Zhai, T. Y. Self-driven WSe_2/Bi_2O_2Se van der Waals heterostructure photodetectors with high light on/off ratio and fast response. *Adv. Funct. Mater.* **2021**, *31*, 2008351.

[54] Yang, M.; Zhang, X. Q.; Zhou, H. X.; Fu, G.; Zhou, X.; Lian, Y. L.; Hao, J. X.; Yu, H.; Zhu, X. Y.; Wang, J. *In situ* preparation of Bi_2O_2Se/MoO_3 thin-film heterojunction array flexible photodetectors. *J. Mater. Chem. C* **2022**, *10*, 15377–15385.

[55] Yu, M.; Fang, C. C.; Han, J. F.; Liu, W. L.; Gao, S. M.; Huang, K. Construction of Bi_2O_2Se/Bi_2Se_3 van der Waals heterostructures for self-powered and broadband photodetectors. *ACS Appl. Mater. Interfaces* **2022**, *14*, 13507–13515.

[56] Kumar, A.; Chakkar, A. G.; Das, C.; Kumar, P.; Sahu, S.; Saliba, M.; Kumar, M. Self-powered broadband photodetectors based on WS_2-anchored MoS_2 with enhanced responsivity and detectivity. *Small* **2025**, *21*, 2502900.